ARTICLE TYPE

# Oscillations and patterns in a model of simultaneous CO and $C_2H_2$ oxidation and $NO_x$ reduction in a cross-flow reactor

**Otto Hadač**[a]**, Martin Kohout**[a]**, Jaromír Havlica**[b,c] **and Igor Schreiber**[a]

A model describing simultaneous catalytic oxidation of CO and $C_2H_2$ and reduction of $NO_x$ in a cross-flow tubular reactor is explored with the aim of relating spatiotemporal patterns to specific pathways in the mechanism. For that purpose, a detailed mechanism proposed for three-way catalytic converters is split into two subsystems, i) simultaneous oxidation of CO and $C_2H_2$, and ii) oxidation of CO combined with $NO_x$ reduction. The ability of these two subsystems to display mechanism-specific dynamical effects is studied initially by neglecting transport phenomena and applying stoichiometric network and bifurcation analyses. We obtain inlet temperature - inlet oxygen concentration bifurcation diagrams, where each region possessing specific dynamics - oscillatory, bistable and excitable - is associated with a dominant reaction pathway. Next, the spatiotemporal behaviour due to reaction kinetics combined with transport processes is studied. The observed spatiotemporal patterns include phase waves, travelling fronts, pulse waves and spatiotemporal chaos. Although these types of pattern occur generally when the kinetic scheme possesses autocatalysis, we find that some of their properties depend on the underlying dominant reaction pathway. The relation of patterns to specific reaction pathways is discussed.

## 1 Introduction

Nonlinear dynamical effects in catalytic reactors including spatiotemporal patterns have been a subject of considerable research activity within past few decades[1]. Multiple steady states and waves have been examined both theoretically and experimentally in a number of studies, most notably CO oxidation observed on the surface of a single Pt crystal[2,3]. Patterns in heterogeneous reactors with a supported catalyst are of great practical interest and have also been extensively studied[4]. The catalytic oxidation of CO displays a broad variety of complex nonlinear dynamics including oscillations on a supported Pt catalyst[5], oscillations on $CuO/Al_2O_3$[6], and periodic and chaotic oscillations on $Pt/Al_2O_3$ pellets[7,8]. Given the considerable nonuniformity of the catalyst properties, experimental difficulties occur in observing well-defined patterns. Nonetheless, theoretical predictions of pattern occurrence in various types of reactors including fixed bed[9,10] and cross-flow catalytic reactors[11] are of great interest in understanding feasible dynamics of reactors used in applications.

A large number of mathematical models has been developed for catalytic converters of exhaust gases differing in the complexity of description of heat and mass transfer, and chemistry. Heck *et al.*[12] used a one-dimensional model and a two-dimensional steady state model to examine dynamics of rapid reactions. Oh and Cavendish[13] studied transient behaviour in a converter after a step change in the inlet temperature. Zygourakis and Aris[14] examined diffusive resistance of the catalytic layer and conditions for multiplicity of steady states. Tronconi and Forzatti[15] compared one- and two-dimensional models of monolithic reactors for selective catalytic reduction of $NO_x$ by $NH_3$. Lie *et al.*[16] studied effects of oscillating feed composition of CO and $O_2$. Pinkas *et al.*[17] and Kirchner and Eigenberger[18] modeled electrically preheated converters to improve catalyst efficiency during the cold start. Balakotaiah *et al.*[19] formulated a simplified model for catalytic reactions in short monoliths. Apart from simplified kinetic schemes, more recent research employs detailed (microkinetic) reaction mechanisms[20–22]. Guthenke *et al.*[23] provide a comprehensive review of approaches to mathematical modelling of catalytic converters.

This work focuses on exploring the range of patterns predicted to occur due to interaction of reactions taking place in a three-way catalytic converter (TWC) with transport phenomena and their relation to mechanistic details. In addition to axial diffusion and convection, a cross-flow of mass along the reactor is used to accentuate the system's ability to generate oscillations and form patterns. Since the chemistry in catalytic converters is complex with many positive and negative feedback loops, reaction network theories prove useful in gaining

*[a] Department of Chemical Engineering, Prague Institute of Chemical Technology, Technická 5, 166 28 Prague 6, Czech Republic. E-mails: martin.kohout@vscht.cz, igor.schreiber@vscht.cz*
*[b] Institute of Chemical Process Fundamentals, Academy of Sciences of the Czech Republic, Rozvojová 135, 165 02 Prague 6, Czech Republic.*
*[c] University of Jan Evangelista Purkinje, České mládeže 8, Ústí nad Labem, 400 96, Czech Republic.*

insight into dynamic behaviour[24]. In this work, the method of stoichiometric network analysis (SNA)[25] is employed. The SNA provides a natural way of decomposing the chemical network into elementary subnetworks and identifies those which are potentially a source of dynamical instabilities[26]. A detailed TWC reaction mechanism[27–29] used in this work can be intuitively decomposed into three subsystems – CO oxidation, $C_2H_2$ oxidation (a prototypical hydrocarbon), and $NO_x$ reduction. However, such a decomposition is not useful in finding whether there are dynamical instabilities. By employing the SNA, Marek *et al.*[30] identified possible sources of oscillatory behaviour in the CO oxidation subsystem of the TWC mechanism, while Hadač and Schreiber[31] examined oscillatory subnetworks occurring due to synergy of all the intuitive subsystems. These oscillatory subnetworks are used below to elucidate bifurcation diagrams for the lumped TWC model and subsequently taken as a basis to examine their role in dynamics when coupled with diffusion and convection.

In Section 2 a reaction-transport model of the TWC is introduced. Section 3 contains a brief summary of our techniques based on the reaction network and bifurcation theories. The results are reported in Section 4.

# 2 A simple reaction-transport model of the TWC

For the purpose of analyzing the interplay between kinetic instabilities in certain subnetworks and diffusion/convection we use a simple two-phase spatially one-dimensional converter-inspired system with mass transfer between the gas and the catalyst layer. The chemistry is described by a detailed kinetic scheme to account for all feasible instabilities due to nonlinear nature of the rate laws. The detailed TWC reaction mechanism[27,28,32] is shown in Table 1. The basic reaction subsystems of CO and $C_2H_2$ oxidation on the active Pt (∗), chemisorption and deposition of $O_2$ on Ce oxides (s), deposition of $CO_2$ on $\gamma$-$Al_2O_3$ ($\gamma$) and reduction of $NO_x$ on Pt sites are indicated by separating lines. Except for the $CO_2$ deposition, all the subsystems are chemically coupled via active Pt sites and species adsorbed on them, which have crucial role in dynamical instabilities. However, our primary interest is in the connection between specific kinetic instabilities and properties of spatiotemporal patterns when the reaction is coupled with diffusion/convection and for that purpose we assume a diffusive cross-flow of reactants along the system. Although the cross-flow is not implemented in industrial catalytic converters, it allows the analysis to begin with the reaction-diffusion-cross-flow system, which admits spatially homogeneous concentration profiles, and the effects of axial convection are studied afterwards. Moreover, the bifurcation phenomena associated with homogeneous solutions

can be well understood by examining the point (lumped) system, retaining only reaction and cross-flow. Therefore prior to formulating the reaction-transport model and analysing the spatiotemporal patterns, we examine the spatially lumped system where the SNA methods can be readily applied and basic bifurcation diagrams indicating chemical instabilities can be constructed.

## 2.1 Lumped model

To understand the dynamics of the TWC reaction kinetics alone, transport phenomena are neglected except for mass transfer between the bulk gas and the gas in the catalytic layer. Consequently, the lumped model of the reactor consists of two compartments — the bulk gas and the gas in pores — with mutual mass exchange complemented by two surface reaction subsystems. It has been shown that even such a simple approximation of the TWC is capable of producing complex dynamical behaviour including stable oscillations, multiplicity of steady states and hysteresis[32]. The corresponding mass balance equations of relevant species in the bulk gas, in the pores of the catalyst, and on the catalyst surface are

$$\frac{dc_i(t)}{dt} = k_{\text{ref}}\frac{T^{\text{in}}}{T^{\text{std}}}(c_i^{\text{in}} - c_i) + \frac{k_c a}{\varepsilon^{\text{g}}}(c_i^{\text{s}} - c_i), \quad (1a)$$

$$\frac{dc_i^{\text{s}}(t)}{dt} = \frac{1}{\varepsilon^{\text{s}}}\sum_{j=1}^{J}\nu_{ij}R_j - \frac{k_c a}{\varepsilon^{\text{s}}(1-\varepsilon^{\text{g}})}(c_i^{\text{s}} - c_i), \quad (1b)$$

$$\frac{d\theta_k(t)}{dt} = \frac{1}{L_{\text{NM}}}\sum_{j=1}^{J}\nu_{kj}R_j, \quad (1c)$$

$$\frac{d\xi_m(t)}{dt} = \frac{1}{L_{\text{OSC}}}\sum_{j=1}^{J}\nu_{mj}R_j, \quad (1d)$$

where $c_i$ and $c_i^{\text{s}}$ are concentrations of the $i$-th species in the bulk gas and in the pores, respectively. Assuming ideal gas law, we obtain the inlet concentrations $c_i^{\text{in}} = y_i^{\text{in}}p/(RT^{\text{in}})$, where $p = 101325$ Pa is the atmospheric pressure, $R = 8.314$ J mol$^{-1}$ K$^{-1}$ is the gas constant and $T^{\text{in}}$ is the inlet temperature. The inlet molar fractions are set to $y_{\text{CO}}^{\text{in}} = 1.22$ %, $y_{\text{CO}_2}^{\text{in}} = 20$ %, $y_{\text{C}_2\text{H}_2}^{\text{in}} = 680$ ppm, $y_{\text{NO}}^{\text{in}} = 1000$ ppm and $y_{\text{NO}_2}^{\text{in}} = 1$ ppm. Symbols $\theta_k$ and $\xi_m$ stand for the coverages of the $k$-th species on noble metal sites (Pt), and the $m$-th species on oxygen storage sites (Ce oxides), respectively. The volumetric mass transfer coefficient $k_c a = 2067$ s$^{-1}$ is the product of the mass transfer coefficient $k_c$ and the specific external surface area $a$, $R_j$ is the rate of $j$-th reaction, $\nu_{ij}$ denotes the stoichiometric coefficient of $i$-th species in $j$-th reaction. The loadings $L_{\text{NM}}$ and $L_{\text{OSC}}$ represent the total concentration of noble metal sites, and oxygen storage sites, respectively. Following our earlier work[30] we use two sets of loadings, a) $L_{\text{NM}} = 40$ mol m$^{-3}$, $L_{\text{OSC}} = 20$ mol m$^{-3}$ and b) $L_{\text{NM}} = 80$ mol m$^{-3}$, $L_{\text{OSC}}$

**Table 1** Detailed reaction scheme of the TWC model. Units used in expressions for reaction coefficients are proper combinations of $s$, $mol\ m^{-3}$, $K$ and $kJ$.

| No. | Reaction | Reaction rate | Reaction coefficients |
|---|---|---|---|
| 1 | $CO + * \rightleftharpoons CO^*$ | $\mathscr{R}_1 = k_1^f L_{NM} c_{CO} \theta_* - k_1^b L_{NM} \theta_{CO^*}$ | $k_1^f = 9\times10^5,\ k_1^b = 5.65\times10^{14} e^{-\frac{113-8.5\theta_{CO}}{RT}}$ |
| 2 | $O_2 + 2* \rightarrow 2O^*$ | $\mathscr{R}_2 = k_2 L_{NM} c_{O_2} \theta_*$ | $k_2 = 1\times10^5$ |
| 3 | $CO^* + O^* \rightarrow CO_2 + 2*$ | $\mathscr{R}_3 = k_3 L_{NM} c_{CO^*} \theta_{O^*}$ | $k_3 = 2.81\times10^{13} e^{-\frac{96.8}{RT}}$ |
| 4 | $CO + O^* \rightleftharpoons OCO^*$ | $\mathscr{R}_4 = k_4^f L_{NM} c_{CO} \theta_{O^*} - k_4^b L_{NM} \theta_{OCO^*}$ | $k_4^f = 4.6\times10^3,\ k_4^b = 248\ e^{-\frac{20.3}{RT}}$ |
| 5 | $OCO^* \rightarrow CO_2 + *$ | $\mathscr{R}_5 = k_5 L_{NM} \theta_{OCO^*}$ | $k_5 = 20.5\ e^{-\frac{12.1}{RT}}$ |
| 6 | $C_2H_2 + * \rightleftharpoons C_2H_2^*$ | $\mathscr{R}_6 = k_6^f L_{NM} c_{C_2H_2} \theta_* - k_6^b L_{NM} \theta_{C_2H_2^*}$ | $k_6^f = 1.32\times10^7,\ k_6^b = 1.11\times10^{11} e^{-\frac{93.5}{RT}}$ |
| 7 | $C_2H_2^* + 2* \rightleftharpoons C_2H_2^{***}$ | $\mathscr{R}_7 = k_7^f L_{NM} \theta_{C_2H_2^*} \theta_*^2 - k_7^b L_{NM} \theta_{C_2H_2^{***}}$ | $k_7^f = 2.5\times10^9 e^{-\frac{44.4}{RT}},\ k_7^b = 2.27\times10^{11} e^{-\frac{125}{RT}}$ |
| 8 | $C_2H_2^* + 3O^* \rightarrow 2CO^* + H_2O + 2*$ | $\mathscr{R}_8 = k_8 L_{NM} \theta_{C_2H_2^*} \theta_{O^*}$ | $k_8 = 9.35\times10^{11} e^{-\frac{151}{RT}}$ |
| 9 | $C_2H_2^{***} + 3O^* \rightarrow 2CO^* + H_2O + 4*$ | $\mathscr{R}_9 = k_9 L_{NM} \theta_{C_2H_2^{***}} \theta_{O^*}$ | $k_9 = 2.25\times10^5 e^{-\frac{161}{RT}}$ |
| 10 | $C_2H_2 + O^* \rightleftharpoons C_2H_2O^*$ | $\mathscr{R}_{10} = k_{10}^f L_{NM} c_{C_2H_2} \theta_{O^*} - k_{10}^b L_{NM} \theta_{C_2H_2O^*}$ | $k_{10}^f = 534,\ k_{10}^b = 5.86$ |
| 11 | $C_2H_2O^* + 2O^* \rightarrow 2CO^* + H_2O + *$ | $\mathscr{R}_{11} = k_{11} L_{NM} \theta_{C_2H_2O^*} \theta_{O^*}$ | $k_{11} = 9730\ e^{-\frac{0.5}{RT}}$ |
| 12 | $O_2 + 2s \rightarrow 2O^s$ | $\mathscr{R}_{12} = k_{12} L_{OSC} c_{O_2} \xi_s$ | $k_{12} = 11.1$ |
| 13 | $CO^* + O^s \rightarrow CO_2 + * + s$ | $\mathscr{R}_{13} = k_{13} L_{NM} c_{CO^*} \xi_{O^s}$ | $k_{13} = 962\ e^{-\frac{11}{RT}}$ |
| 14 | $C_2H_2^* + 3O^s + * \rightarrow 2CO^* + H_2O + 3s$ | $\mathscr{R}_{14} = k_{14} L_{NM} \theta_{C_2H_2^*} \xi_{O^s}$ | $k_{14} = 1.76\times10^{12} e^{-\frac{124}{RT}}$ |
| 15 | $CO_2 + \gamma \rightleftharpoons CO_2^\gamma$ | $\mathscr{R}_{15} = k_{15}^f L_{SUP} c_{CO_2} \delta_\gamma - k_{15}^b L_{SUP} \delta_{CO_2^\gamma}$ | $k_{15}^f = 10.1,\ k_{15}^b = 112 e^{-\frac{5.26}{RT}}$ |
| 16 | $NO + * \rightleftharpoons NO^*$ | $\mathscr{R}_{16} = k_{16}^f L_{NM} c_{NO} \theta_* - k_{16}^b L_{NM} \theta_{NO^*}$ | $k_{16}^f = 3.63\times10^5,\ k_{16}^b = 3.04\times10^{10} e^{-\frac{83.2}{RT}}$ |
| 17 | $NO^* + * \rightarrow N^* + O^*$ | $\mathscr{R}_{17} = k_{17} L_{NM} \theta_{NO^*} \theta_*$ | $k_{17} = 2.19\times10^5 e^{-\frac{45.8}{RT}}$ |
| 18 | $NO^* + N^* \rightarrow N_2O^* + *$ | $\mathscr{R}_{18} = k_{18} L_{NM} \theta_{NO^*} \theta_{N^*}$ | $k_{18} = 2.16\times10^5 e^{-\frac{38.3}{RT}}$ |
| 19 | $N_2O^* \rightarrow N_2O + *$ | $\mathscr{R}_{19} = k_{19} L_{NM} \theta_{N_2O^*}$ | $k_{19} = 2.71\times10^6 e^{-\frac{45.3}{RT}}$ |
| 20 | $N_2O^* \rightarrow N_2 + O^*$ | $\mathscr{R}_{20} = k_{20} L_{NM} \theta_{N_2O^*}$ | $k_{20} = 4640 e^{-\frac{20.1}{RT}}$ |
| 21 | $N^* + N^* \rightarrow N_2 + 2*$ | $\mathscr{R}_{21} = k_{21} L_{NM} \theta_{N^*}^2$ | $k_{21} = 4.08\times10^8 e^{-\frac{56.6}{RT}}$ |
| 22 | $NO + O^* \rightleftharpoons NO_2^*$ | $\mathscr{R}_{22} = k_{22}^f L_{NM} c_{NO} \theta_{O^*} - k_{22}^b L_{NM} \theta_{NO_2^*}$ | $k_{22}^f = 585,\ k_{22}^b = 2270 e^{-\frac{28.6}{RT}}$ |
| 23 | $NO_2^* \rightleftharpoons NO_2 + *$ | $\mathscr{R}_{23} = k_{23}^f L_{NM} \theta_{NO_2^*} - k_{23}^b L_{NM} c_{NO_2} \theta_*$ | $k_{23}^f = 2.18\times10^8 e^{-\frac{97.8}{RT}},\ k_{23}^b = 5.34\times10^6$ |

= 0.1 mol m$^{-3}$; $\varepsilon^g = 0.917$ is the void fraction of the reactor, $\varepsilon^s = 0.8$ is the porosity of the catalytic layer (washcoat), $k_{ref} = 20.8$ s$^{-1}$ is the space velocity (at a reference temperature $T^{std}$) and $t$ is time. We choose $T^{in}$ and $y_{O_2}^{in}$ as variable parameters to be used in numerical continuations and bifurcation analysis[33]. Since we primarily intend to focus on the role of kinetic rather than thermokinetic autocatalysis, we assume isothermal conditions. This approximation has been also used in our earlier work[30]. Based on the estimated adiabatic temperature rise one can readily determine that the oscillations in temperature accompanying patterns examined below would cause variation in reaction rate that is at least an order of magnitude lower than that caused by oscillations of autocatalytic chemical species thus implying primary role of kinetic autocatalysis.

## 2.2 Spatially distributed model
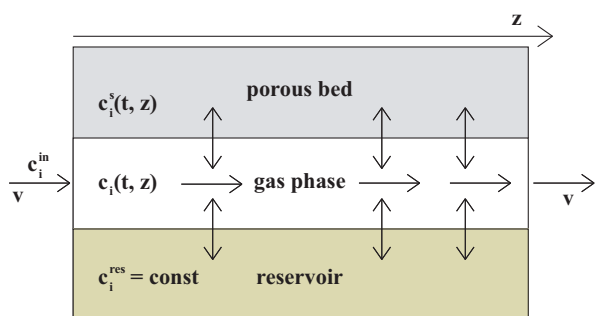


**Fig. 1** Schematic figure of a 1D tubular reactor with a cross-flow.

Fig. 1 shows schematically the system: the channel through which the gas flows is in direct contact with the porous catalytic layer on one side and membrane mediated contact with a reservoir/pool of reactants on the other side. Mass transfer is assumed between the gas and the catalytic layer as well as between the gas and the pool. For simplicity, both the catalytic layer and the gas channel are assumed sufficiently thin so that transverse diffusion in either phase is fast. On the other hand, longitudinal diffusion in the catalytic layer is assumed negligible relative to the axial diffusion/dispersion in the gas. The reservoir is assumed well mixed (e.g., a channel with rapidly recycling inlet gas). In addition, isothermal conditions and plug flow are assumed. This type of reactor with a cross-flow (CFR) has been extensively used previously to study pattern formation in a system with exothermic first order reaction, see[9–11] and references therein).

A spatially one-dimensional model based on local mass bal-

ances of each species in the CFR then reads

$$
\frac{\partial c_i(t,z)}{\partial t} + v\frac{\partial c_i(t,z)}{\partial z} = D_i\frac{\partial^2 c_i(t,z)}{\partial z^2} + P(c_i^{res} - c_i) +
$$
$$
+ \frac{k_c a}{\varepsilon^g}(c_i^s - c_i), \tag{2a}
$$

$$
\frac{\partial c_i^s(t,z)}{\partial t} = \frac{1}{\varepsilon^s}\sum_{j=1}^{J}\nu_{i,j}R_j -
$$
$$
- \frac{k_c a}{\varepsilon^s(1-\varepsilon^g)}(c_i^s - c_i), \tag{2b}
$$

$$
\frac{\partial \theta_k(t,z)}{\partial t} = \frac{1}{L_{NM}}\sum_{j=1}^{J}\nu_{k,j}R_j, \tag{2c}
$$

$$
\frac{\partial \xi_m(t,z)}{\partial t} = \frac{1}{L_{OSC}}\sum_{j=1}^{J}\nu_{m,j}R_j. \tag{2d}
$$

In addition to notation used in eqn (1a)–(1d), $v$ is the convective velocity, $D_i$ is the diffusion/dispersion coefficient and $P$ is the volumetric mass transfer coefficient for the cross-flow. When examining the reaction–diffusion system ($v = 0$), no-flux boundary conditions ($\frac{\partial c_i}{\partial z} = 0$) on both sides are used. Upon adding the convective flow, the no-flux boundary condition at the inlet extends to the Danckwerts boundary condition ($vc_i^{in} = vc_i - D_i\frac{\partial c_i}{\partial z}$).

The value of $P$ is set equal to the (temperature adjusted) space velocity used in the lumped model and the reservoir concentration $c_i^{res}$ is set equal to $c_i^{in}$ so that the dynamics in the CFR corresponds to the lumped model when axial transport is neglected. In other words, for the system without convection there is a spatially homogeneous solution of eqn (2a)–(2d) corresponding to any solution of eqn (1a)–(1d). Homogeneous steady states are of particular interest as their bifurcation behaviour is closely linked to that of the lumped system. In the presence of convection, the inlet generates a steep gradient zone near the entrance that violates the homogeneity and can serve as a source of wave patterns. In addition, wave patterns can be readily initiated by properly choosing an inhomogeneous initial condition. In order to observe the wave patterns immediately from the start of simulations even in the absence of convection, the initial condition for the concentrations of species has been chosen as follows: the first half of the reactor length corresponds to a reference high-conversion steady state of the lumped system, while the other half corresponds to a reference low-conversion steady state. This choice is favorable for occurrence of a wave initiated in the middle of the system.

According to our assumptions, axial diffusion within the catalytic layer is neglected both on the solid surface and in the stagnant gas. Therefore only species in the mobile gas phase are subject to axial diffusion/dispersion. For simplicity, we set the diffusion coefficients for all species in gas equal to

$D_i = 0.1$ cm$^2$ s$^{-1}$; this value corresponds to diffusivities (possibly Taylor dispersion enhanced) in gas at temperatures 500-600 K typically occurring in the converter. All the diffusing chemical species have diffusivities differing from one another by at most 20 %. Therefore we assume a species independent value for $D_i$s, and also for the cross-flow coefficient $P$. We did verify that the patterns are robust to variations in $D_i$.

## 3 Techniques

### 3.1 Numerical techniques

The lumped system given by eqn (1a)–(1d) is examined by using a true arclength numerical continuation method[33] implemented in a software tool Cont[34,35]. This tool enables us to construct bifurcation diagrams and determine the number of steady states, their stability and bifurcations within the parameter plane $T^{in}$ - $y^{in}$.

The spatially distributed system represented by eqn (2a)–(2d) was discretised in space and solved as a system of ordinary differential equations by the LSODE solver embedded within Cont. We used a grid of 800 intervals and set the relative tolerance of the ODE solver to $10^{-6}$.

### 3.2 Stoichiometric network analysis

A chemical network is a set of $n$ chemical species and $m$ chemical reactions with known kinetics. The time evolution in a spatially homogeneous system at constant temperature is based on mass balance equations that may be written in a compact form as

$$\frac{dc}{dt} = Nr(c), \tag{3}$$

where $c$ is the $n$-vector of concentrations of the species, $r(c)$ is the $m$-vector of the rate laws and $N$ is the stoichiometric matrix. Eqn (3) may be readily extended to represent a flow system provided that $N$ and $r$ involve pseudoreactions corresponding to inflows and outflows (zero and first order terms, respectively). According to the stoichiometric network analysis (SNA), stability of steady states of eqn (3) can be conveniently analyzed by determining the structure of the null space of $N$ using convex analysis and examining the Jacobi matrix upon reformulating the system in terms of convex parameters[25].

In the first step the set of steady state reaction rate vectors corresponding to extreme (or elementary) subnetworks is found. Any steady state reaction rate vector in the reaction network can be obtained as a convex combination of the rate vectors of the extreme subnetworks, which in geometrical terms are edges of an open convex cone in the nonnegative orthant of the null space. Certain k-tuples of the edges span faces of

the cone constituting thus a natural hierarchy of increasingly complex subnetworks.

In the second step linear stability analysis is applied to edges/faces to reveal mechanistic sources of multiple steady states or oscillatory behaviour. The stability of a subnetwork is indicated by principal subdeterminants of a matrix closely related to the Jacobi matrix $\frac{d(Nr(c))}{dc}$. Of particular interest are oscillatory instabilities occurring via Hopf bifurcation. Namely, the subnetworks accounting for oscillations can be used to classify the chemical mechanism according to the arrangement of positive and negative feedback loops and to determine the role of species in the oscillations[36,37]. At the Hopf bifurcation or close to it, various methods can be applied to determine the role, for example, by determining mutual phase shifts of chemical species[26], which can be calculated from the eigenvectors associated with the pair of pure imaginary eigenvalues of the Jacobi matrix. Of interest here are three types of species playing an essential role in the oscillations: type X is the autocatalytic species that appears in the autocatalytic loop; type Z provides negative feedback controlling the oscillations and type Y removes the type X species from the autocatalytic cycle.

Waves in spatially distributed media can occur due to nonlinear chemical reactions coupled with transport phenomena. Phase waves, travelling pulses and front waves are the simplest cases. Since pulses are associated with excitability, fronts with bistability and phase waves with oscillations in the lumped system, the bifurcation diagram can be used to indicate the regions where waves in the cross-flow reactor can be expected.

## 4 Results

In addition to sole CO oxidation subsystem, there are two other intuitive subsystems of the TWC mechanism: simultaneous oxidation of CO and $C_2H_2$, and simultaneous CO oxidation and $NO_x$ reduction. These simplified cases result from assuming that either $NO_x$ or hydrocarbons are absent from the inlet gas stream, respectively. Our primary goal is to examine to what extent the instabilities in these major subsystems differ and how is this difference reflected in the dynamics under the CFR conditions. Both subsystems are examined in detail using the SNA elsewhere[31], here we build on those results to find the relations between unstable oscillatory subnetwork and waves in the spatially distributed system.

### 4.1 Subsystem I – oxidation of CO and $C_2H_2$

Fig. 2 shows the bifurcation diagram in the parameter plane of the inlet molar fraction of oxygen $y_{CO}^{in}$ and the temperature $T^{in}$ for the lumped system. Here we use the first of the two choices of loadings, mentioned earlier, namely $L_{NM} = 40$ mol m$^{-3}$, $L_{OSC} = 20$ mol m$^{-3}$. It turns out that $C_2H_2$ oxidation

requires the oxygen adsorbed on the cerium sites, thus $L_{OSC}$ has to be sufficiently large to observe sizeable regions of oscillatory dynamics.

The closed bow-shaped curve of the saddle-node bifurcations encloses a region of multiple steady states. The stoichiometric amount of oxygen required for complete removal of CO and $C_2H_2$ corresponds to $y_{O_2}^{in} = 0.78$ mol. %, which is dividing the bifurcation diagram into sub- and superstoichiometric domains. In addition, the Hopf bifurcation curves terminating at the saddle-node bifurcation via Bogdanov-Takens points approximately mark two regions of stable oscillatory dynamics outside the multiple steady state region and two subregions of a unique stable steady state within the multiple steady state region. More precisely, the oscillatory domains are slightly larger than indicated by the Hopf and saddle-node curves; the boundary of the oscillatory domain adjacent to the multiple steady state domain is determined partly by a saddle-node-infinite-period bifurcation (and therefore by the saddle-node curve) and by a saddle-loop bifurcation[35], but in Fig. 2 the corresponding curves practically coincide. In addition, the Hopf bifurcation is mostly subcritical and thus the boundary of the oscillatory domain not adjacent to the region of multiple steady states is delimited by curves of saddle-node bifurcation of limit cycles, but again, these boundaries nearly coincide with the Hopf bifurcation curves.

The dynamics within the two subregions of a unique stable steady state within the multiple steady state region is excitable, i.e., a small but finite perturbation of the steady state causes a large excursion before returning to the steady state. There is bistability elsewhere in the region of the multiple steady states. More remarkably, the two regions of stable oscillations are distinguished by occurring in the sub- and superstoichiometric regions. The same observation holds for the excitability, whereas the region of bistability falls within the substoichiometric domain.

These observations can be elucidated by using the SNA as briefly outlined in Section 3.2 (see refs[26,36] for further details). The CO & $C_2H_2$ network with the two embedded oscillatory subnetworks can be conveniently represented by the network diagram shown in Fig. 3. Here each reaction along with stoichiometry and reaction orders is displayed as a multi-tail/multi-head arrow with the number of feathers/barbs indicating stoichiometric coefficients of reactants/products and, additionally, the number of left feathers indicate the reaction order of the corresponding reactant. In the substoichiometric region the dominant process is as follows: upon adsorption of oxygen on Pt sites the gaseous $C_2H_2$ reacts with O* via step 10 and the intermediate species $C_2H_2O$* is successively oxidised to CO* and $CO_2$ via steps 11 and 13 that involve oxygen adsorbed both on Pt and Ce sites. The hydrocarbon in the gas interacts with the adsorbed oxygen - a process known as Eley-Rideal mechanism. A detailed analysis of the role of species[31]
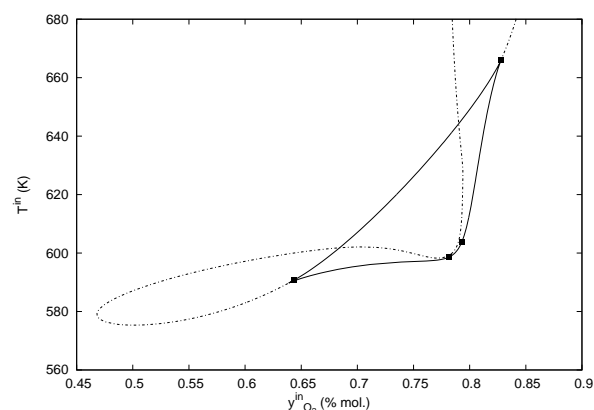


**Fig. 2** Bifurcation diagram for CO and $C_2H_2$ oxidations in the inlet molar fraction of oxygen $y_{O_2}^{in}$ – input temperature $T^{in}$ plane; full-line – curve of saddle-node bifurcation points, dashed line – curve of Hopf bifurcation points, squares – Bogdanov-Takens points.

further reveals that the autocatalytic cycle is formed by linking three type X species *, O* and CO*, while the negative feedback is provided by the flow-controlled availability of oxygen (type Z species) via step 2 and $C_2H_2$ plays the role of the exit species (type Y) via step 10. Notice that the autocatalytic cycle consumes oxygen adsorbed on Ce sites provided by step 12. In the superstoichiometric region there is a different source of the oscillatory instability. Here the dominant process involves adsorption of both $O_2$ and $C_2H_2$ on Pt sites prior their interaction. More specifically, the autocatalytic loop includes the species *, $C_2H_2$* and CO* via the steps 6, 8 and 13. This type of interaction is known as Langmuir-Hinshelwood mechanism. As in the previous case, this necessitates the involvement of Ce site used in step 13. When compared, the roles of the negative feedback species and the exit species in the two submechanisms are exchanged, here $C_2H_2$ (type Z) is controlling the oscillations via step 6 and $O_2$ (type Y) removes * from the autocatalytic cycle via the exit reaction 2.

Understanding of the outlined mechanistic features allows for interpretation of the wave patterns in the reaction-diffusion-convection system (2a)–(2d). In correspondence with the bifurcation diagram in Fig. 2, two regions of phase waves/bulk oscillations associated with two regions of stable oscillatory dynamics in the lumped system (1a)–(1d) were found. The superstoichiometric oscillatory region is marked by transient phase waves slowly leading to synchronised bulk oscillations with a low frequency and high mean conversion of CO, see Fig. 4a. On the other hand the substoichiometric oscillatory region displays lower mean conversion transient phase waves slowly approaching bulk oscillations with a high frequency (Fig. 4b). The difference in frequencies is signifi-
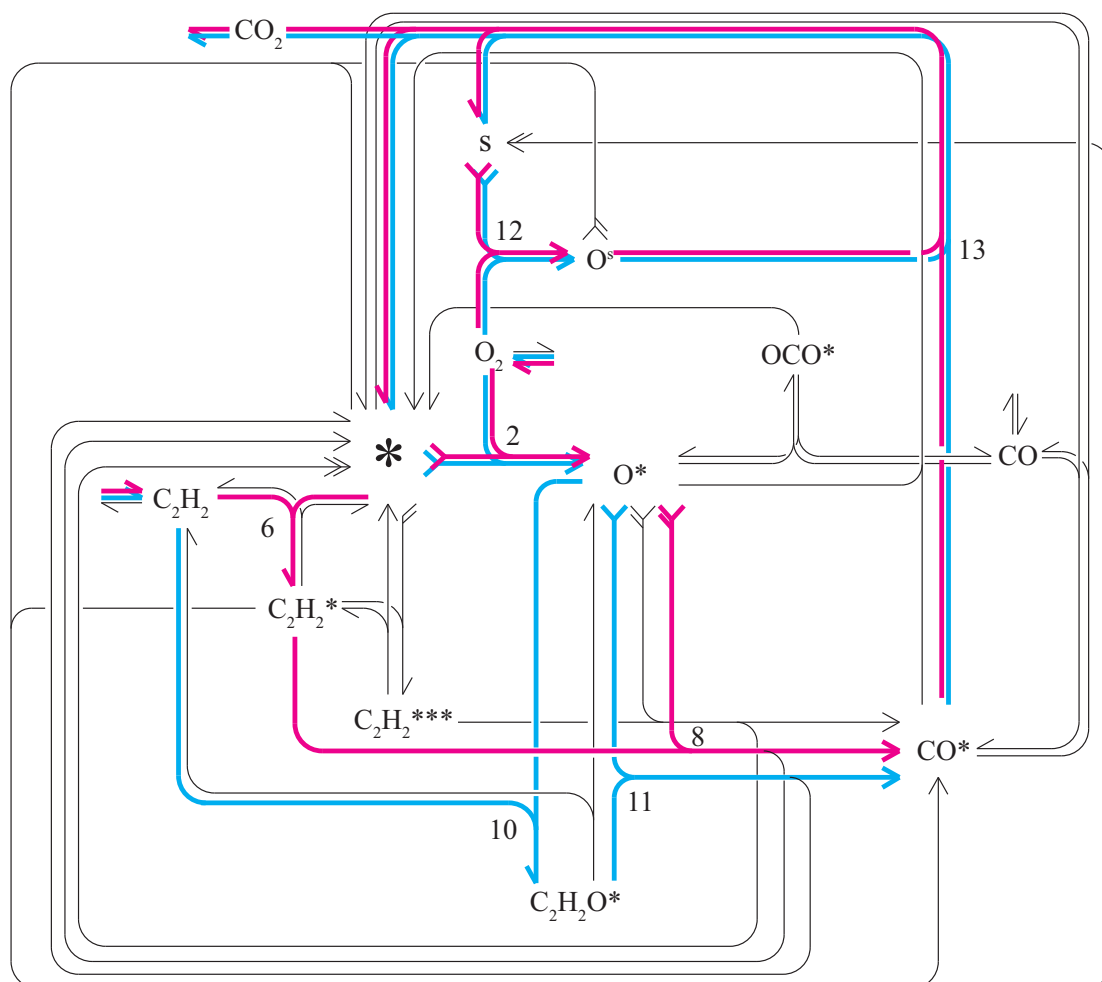
**Fig. 3** Stoichiometric network of CO & $C_2H_2$ oxidation subsystem. Blue line - dominant substoichiometric oscillatory subnetwork, red line - dominant superstoichiometric oscillatory subnetwork. Reactions in the dominant subnetworks are labelled by numbers used in Table 1

cant and can be explained by referring to the inflow rates of the negative feedback species. In the substoichiometric region, $O_2$ is the type Z species with the inflow rate by an order of magnitude larger than that for $C_2H_2$ - the type Z species in the superstoichiometric region. Therefore, within each cycle, the recovery phase following the fast autocatalytic phase is much shorter in the former case, which accounts for the higher frequency. In addition, the phase waves in the superstoichiometric region in the vicinity of the Hopf bifurcation display a remarkable spatiotemporal pattern where the bulk oscillations occur alternately in two segments of the reactor, see Fig. 4c. This transient dynamics is evoked because of our specific initial condition (one half of the system at the lower steady state of the lumped system and the other at the upper one) and slowly evolves into alternating travelling pulses. This feature is found only near the Hopf bifucation and it does not depend on the specific kinetics, because a similar pattern occurs in the CO & $NO_x$ subsystem discussed later and also in unrelated kinetic schemes[38].

In the region of multiple steady states above the Hopf bifurcation curve in the superstoichiometric region only one steady state is stable and it is excitable, which leads to the occurrence of travelling pulses in the CFR (Fig. 5a). With our choice of the initial condition, there is a pair of travelling high-conversion pulses in the absence of convection. The repeated firing of pulses hints at the proximity of oscillatory dynamics associated with the Hopf bifurcation. The number of repeated firings and the wave velocity can be manipulated by applying the convective flow. Negative convective flow (Fig. 5b) speeds up the pulses, stabilises their velocity and allows for a higher number of repeated firings.

The region of two coexisting stable steady states in Fig. 2 is delimited by the curve of saddle-node bifurcation from top-left and by the curves of Hopf bifurcation from the right and from the bottom. As expected, this region of bistability in the lumped system corresponds to travelling front waves in the CFR. Depending on the choice of parameters, the travelling front moves either towards the inlet, in which case it switches from a lower CO-conversion steady state to a higher CO-conversion steady state ("ignition" front) or the wave direction is reverse ("extinction" front), depending on the parameter choice within the bistable region. As before, the wave velocity can be speeded up or slowed down by adding convective flow correspondingly. The convective flow can even be used to reverse the direction of front movement.

Finally, Fig. 6 displays a complex spatiotemporal patterns found within the region of substoichiometric oscillatory dynamics in the absence of convective flow. The pattern is initiated as a slowly broadening instability acquiring eventually the form of irregular modulated phase waves.

The overview of the wave/pattern dynamics is shown in Fig. 7, where the bifurcation diagram for the lumped system in



**(a)**

**(b)**

**(c)**
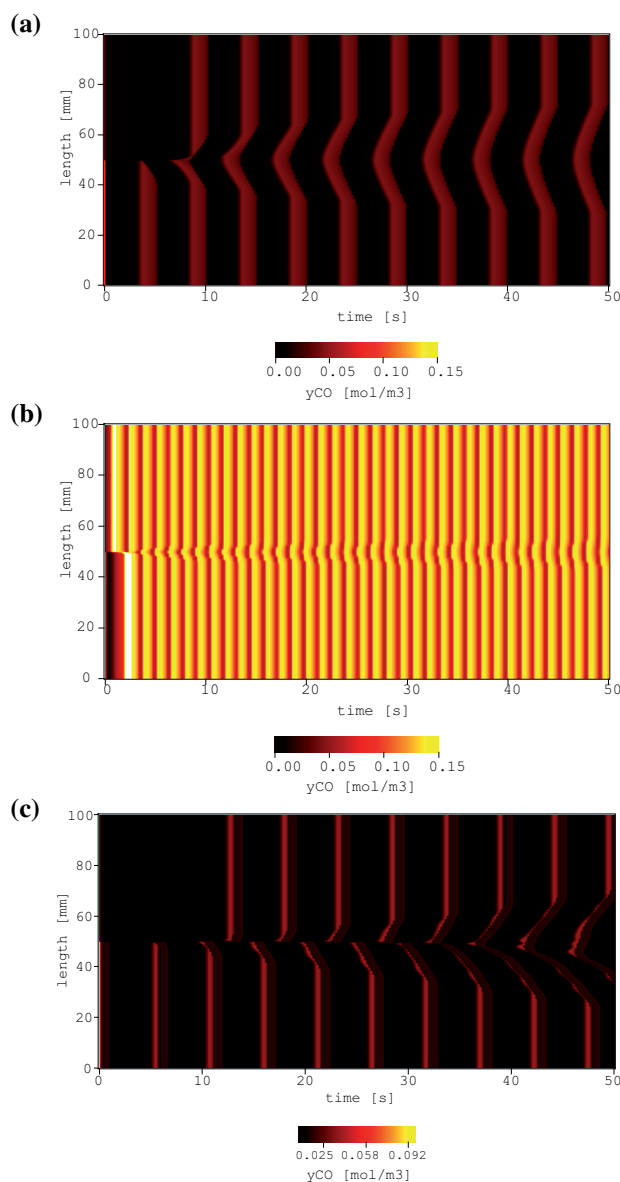
**Fig. 4** The space-time plot of phase waves synchronised into bulk oscillations; the inlet oxygen concentration (a) – $y_{O_2}^{in}$ = 0.81 mol. % and the temperature $T^{in}$ = 658.0 K, (b) – $y_{O_2}^{in}$ = 0.50 mol. % and $T^{in}$ = 580.0 K, $v = 0$, (c) – $y_{O_2}^{in}$ = 0.80 mol. % and $T^{in}$ = 658.0 K, $v = 0$. The colour bar indicates the level of concentration of CO.

Fig. 2 is complemented by marking the regions of spatiotemporal dynamics. Clearly, the pulse waves occur only in a limited part of the two subregions of multiple steady states where only one stable steady state occurs. Thus excitability in the lumped system does not necessarily extend to pulse waves in the distributed system. The top-left region of front waves (bistability in the lumped system) corresponds to the "igni-

**(a)**



**(b)**
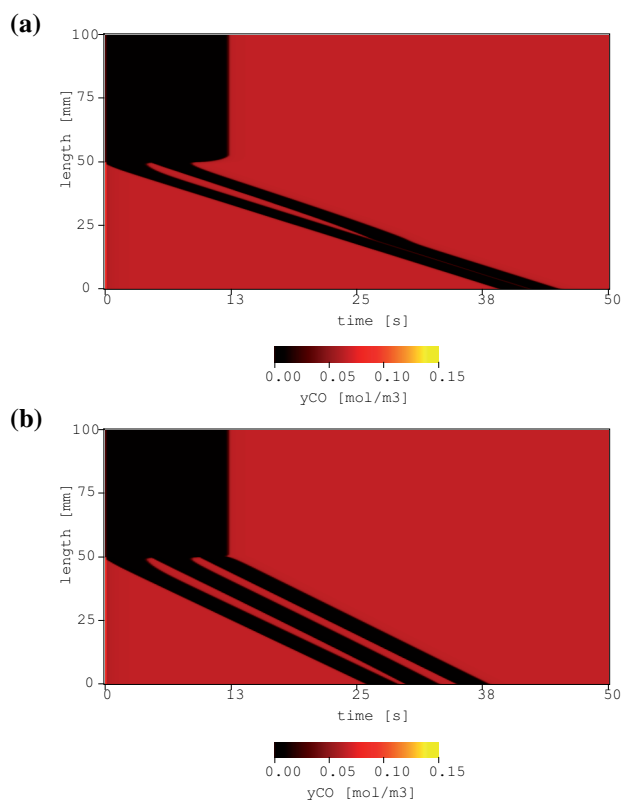


**Fig. 5** The space-time plot of the spontaneously generated travelling pulses; the inlet oxygen concentration $y_{O_2}^{in} = 0.80$ mol. % and the temperature $T^{in} = 640.0$ K, (a) – no convective flow, (b) – $v$ = -1.0 mm/s.
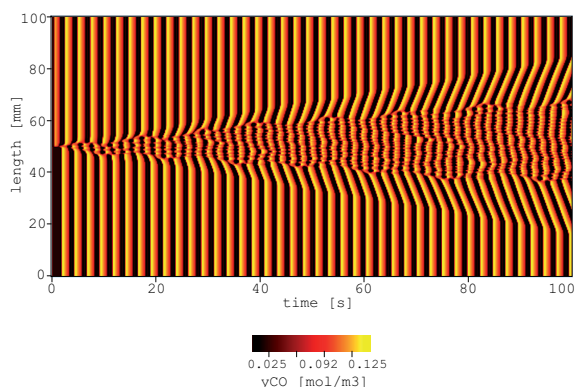


**Fig. 6** The space-time plot of spatiotemporal chaotic pattern; the inlet oxygen concentration $y_{O_2}^{in} = 0.60$ mol. % and the temperature $T^{in} = 590.0$ K, $v = 0$.

tion" fronts under no convection and the complementary region corresponds to the "extinction"fronts. Since the entire

region of fronts falls within the substoichiometric domain, the governing mechanism is of the Eley-Rideal type for each of the two dominating alternative states.
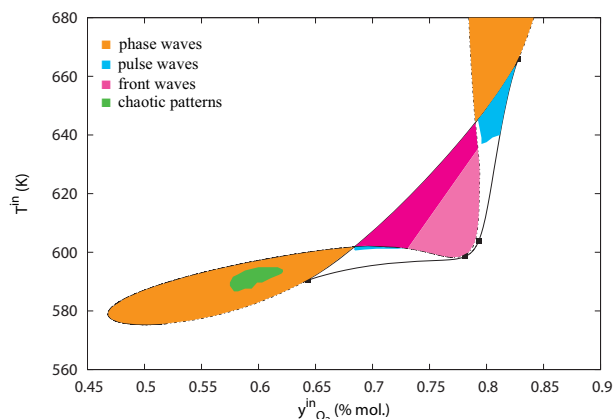


**Fig. 7** Bifurcation diagram for CO and $C_2H_2$ oxidations in the inlet molar fraction of oxygen $y_{O_2}^{in}$ – input temperature $T^{in}$ plane; regions with different dynamics.

### 4.2 Subsystem II – oxidation of CO and reduction of $NO_x$

The bifurcation behaviour for the lumped system in the absence of hydrocarbons is shown in Fig. 8 where the same parameters (the inlet molar fraction of oxygen $y_{CO}^{in}$ and the temperature $T^{in}$) were used. The diagrams in Fig. 8a and 8b differ in the chosen ratio of the loading capacities of the Pt and Ce sites. Figs. 2 and 8a are directly comparable, having the same ratio. An immediate observation is that the CO & $C_2H_2$ subsystem exhibits multiple steady states in a single domain at temperatures from 570 K to 670 K, whereas the CO & $NO_x$ subsystem shows multiple steady states in two partly overlapping but distinct domains, one of them in a significantly lower temperature range (between 450 and 530 K), the other within a comparable temperature range (from 500 K to 640 K). Another important observation is that the oscillations appear to be associated mainly with the multiple steady states region at the lower temperature range. We found that by increasing the ratio of the loading capacities $L_{NM}/L_{OSC}$ the high-temperature domain diminishes and eventually disappears, see Fig. 8b, while the low-temperature domain remains virtually unchanged and two distinct oscillatory regions are adjacent to it. This implies that oscillations in the CO & $NO_x$ subsystem do not involve the Ce sites, unlike in the previous case. Further we therefore examine the system corresponding to Fig. 8b.

The bifurcation diagram in Fig. 8b displays two separate regions of bistability within the region of multiple steady states, a vertical one within the cusp region extending down, and a horizontal one within the cusp region extending to the left.

**(a)**



**(b)**
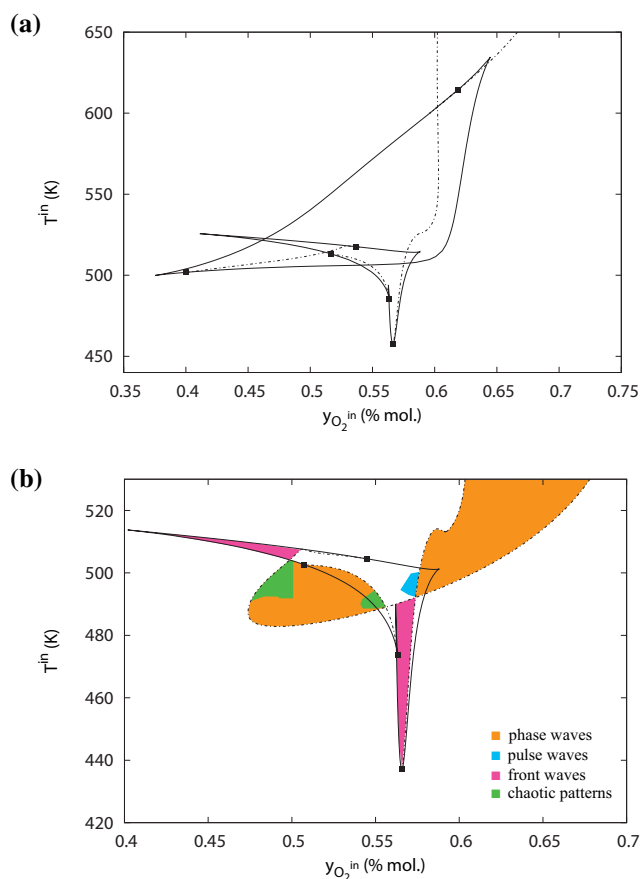


**Fig. 8** Bifurcation diagram for CO oxidation and $NO_x$ reduction in the inlet molar fraction of oxygen $y_{O_2}^{in}$ – input temperature $T^{in}$ plane, (a) $L_{NM}/L_{OSC} = 40.0/20.0$, (b) $L_{NM}/L_{OSC} = 80.0/0.1$; full-line – curve of saddle-node bifurcation points, dashed line – curve of Hopf bifurcation points, squares – Bogdanov-Takens points.

Between them and above the Hopf bifurcation curve, only a high CO-conversion steady state is stable and excitable, while only the lower-conversion steady state is stable and excitable to the right of the vertical bistable region. The stoichiometric amount of oxygen required for complete oxidation of CO and complete reduction of $NO_x$ for the network corresponds to $y_{CO}^{in} = 0.56$ mol. %. As in the previous subnetwork, this value can be used to distinguish the two oscillatory regions in Fig. 8b. The substoichiometric oscillatory region can be subdivided into a larger part where the steady state is unique and unstable and a smaller part within the multiple steady state region separated from the stable steady state by the Hopf bifurcation. The superstoichiometric oscillatory region is enclosed by two Hopf bifurcation curves directed up and to the right from their intersection within the multiple steady state region. The bifurcation diagram differs significantly from that for the CO & $C_2H_2$ subsystem, which brings about different wave

pattern arrangement already indicated in Fig. 8b and will be discussed below after summarizing the main features of the reaction network.

The subnetworks causing the oscillatory instabilities[31] are indicated in Fig. 9. The dominant subnetwork of the substoichiometric oscillator and the superstoichiometric one partly overlap (reactions 1, 3, 16 and 17). The nonoverlapping parts correspond to reduction of $NO_x$ to $N_2$ in the former and to $N_2O$ in the latter oscillator. The autocatalytic cycle in the substoichiometric system is mediated by steps 1 and 3 linking the type X species * and CO*, whereas in the superstoichiometric oscillator there are two autocatalytic cycles operating in synergy: the first one is the same as in the previous case and an additional one proceeding via steps 17 and 18 linking the species * and N*. Because the two oscillators share one of the autocatalytic cycles they are quite similar. The main difference is that the superstoichiometric case implies only partial use of oxygen from NO to oxidise CO via the pathway 16, 17 and 3, and involves production of $N_2O$ via steps 18 and 19. This $N_2O$ pathway in turn implies the second autocatalytic loop with N* and * as the autocatalytic species. Although from the application viewpoint the difference is significant, from the mechanistic viewpoint it is minor, the role of the crucial species remains the same: * and CO* are of type X, NO is of type Y and CO is type Z. Thus the negative feedback is controlled by the same species unlike in the case of CO & $C_2H_2$ sub- and superstoichiometric oscillators and the oscillatory period and amplitude are expected not to differ significantly.

Wave patterns for the CO & $NO_x$ subsystem are more rich than those for the CO & $C_2H_2$ subsystem. The basic types of patterns including phase waves/bulk oscillations, travelling solitary pulses and travelling fronts can be found in the corresponding parts of the bifurcation diagram. Transient phase waves tending asymptotically to bulk oscillations occur within the two oscillatory regions. As indicated by the reaction network analysis, the role of species in the sub- and superstoichiometric oscillations are identical for most of the major species involved. Therefore, unlike in the previous subsystem, the period of bulk oscillations is nearly the same in both regions. In particular, the type Z species in both cases is CO, which has the same inflow rate. The solitary pulse waves occur in the central part of the region of multiple steady states, where just one of them is stable but only under the superstoichiometric conditions. Travelling fronts occur in two separate regions of bistability; interestingly, they are of extinction type in both regions even though the horizontal one falls within the sub- and the vertical one within the superstoichiometric domain. Nonetheless, the similarity of dynamics is consistent with the similarity of the underlying dominant subnetworks.

Remarkably, several types of more complex spatiotemporal patterns exist. One type involves composite dynamics combining bulk oscillations and pulse waves. These dynamical
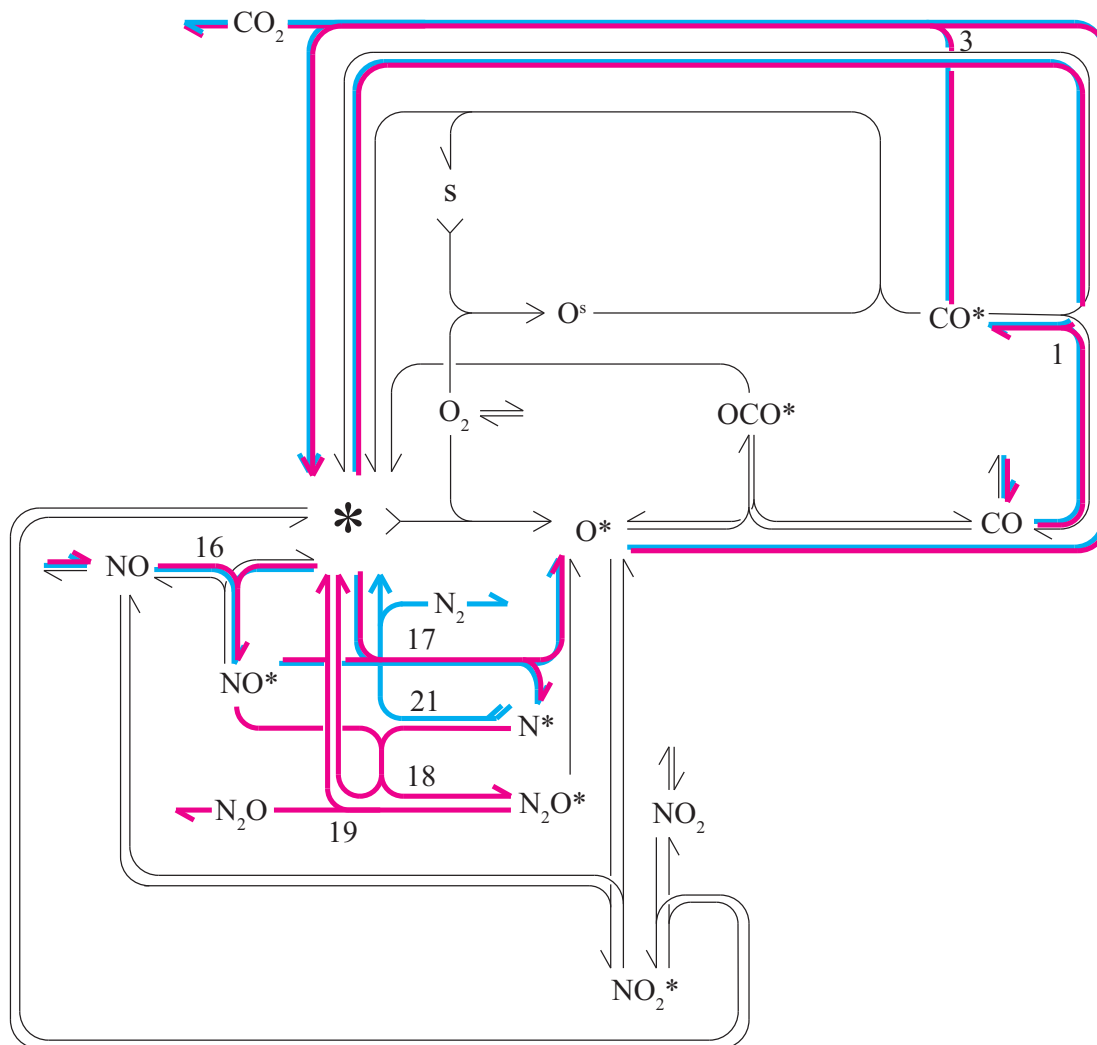
**Fig. 9** Stoichiometric network of CO oxidation & NO$_x$ reduction subsystem. Blue line - dominant substoichiometric oscillatory subnetwork, red line - dominant superstoichiometric oscillatory subnetwork. Reactions in the dominant subnetworks are labelled by numbers used in Table 1

regimes are found on both sides of the Hopf bifurcation curve marking the borderline between the region of pulse waves and the region of bulk superstoichiometric oscillations. Fig. 10 shows patterns on the right of the borderline. In the absence of convective flow, the pattern is characterised by alternating bulk oscillations in each half of the reactor slowly developing into alternating pulse waves moving from the center to both ends (Fig. 10a). This pattern is reminiscent of the pattern shown in Fig. 4c that occurs under analogous constraints. When convection along the reactor is present in addition to the cross-flow, the pattern eventually evolves into irregularly repeated pulse waves initiated at the entrance of the CFR (Fig. 10b). Dynamics on the other side of the borderline is displayed in Fig. 11. When our specific initial condition is applied in the absence of convective flow, first half of the system (initially at low conversion of CO) shows bulk oscillations, while the other half supports pulse waves corresponding to excitations of the high-conversion steady state (Fig. 11a). When convection is added, the pattern slowly evolves into irregular pulse wave trains travelling down the reactor (Fig. 11b).



**(a)**



**(b)**
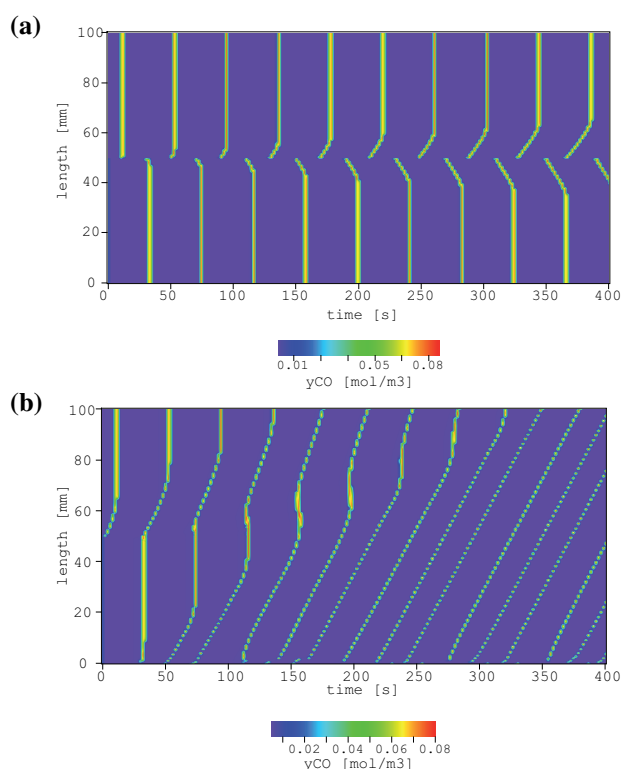
**Fig. 10** The space–time plot phase waves synchronised into bulk oscillations; the inlet oxygen concentration $y_{O_2}^{in} = 0.576$ mol. % and the temperature $T^{in} = 497.0$ K, (a) – $v = 0$, (b) – $v = -10$ mm/s.

Finally, another type of complex patterns is confined to two subregions within the substoichiometric oscillatory region

**(a)**



**(b)**
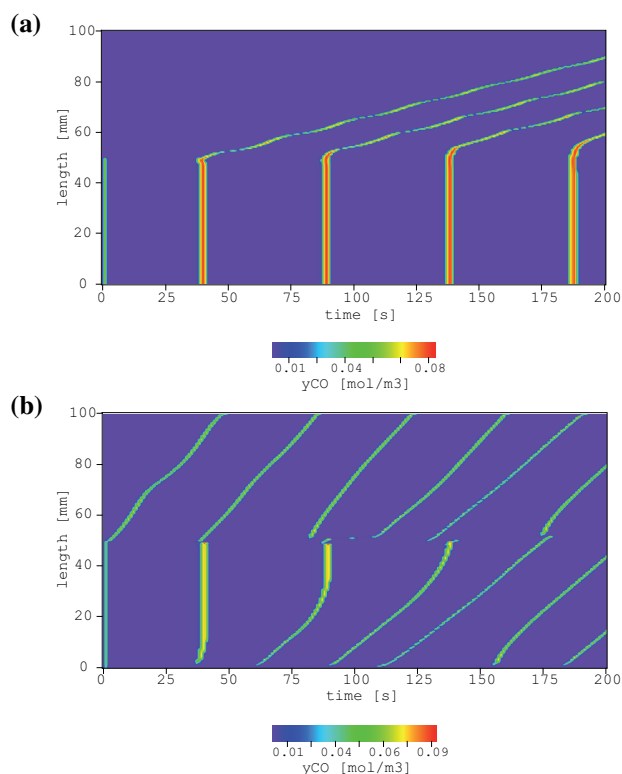


**Fig. 11** The space-time plot of the spontaneously generated travelling pulses; the inlet oxygen concentration $y_{O_2}^{in} = 0.575$ mol. % and the temperature $T^{in} = 497.0$ K, (a) – $v = 0$, (b) – $v = -10$ mm/s.

(Fig. 8b). These patterns are distinctly chaotic, marked by repeatedly occurring local instabilities that disrupt the initially forming bulk oscillations, see Fig. 12. The two subtypes differ by durations of the high-conversion and the low-conversion phases. The dark domains in Fig. 12a are much larger both in space and time directions than those in Fig. 12b. The former pattern corresponds to higher inflow of oxygen, which supports longer phase of high conversion but from the mechanistic point of view, the oscillations are generated by the same type of oscillator.

When convective flow is applied, the size of both chaotic regions in Fig. 8b is enlarged, i.e. convective flow supports the occurrence of complex spatiotemporal patterns. In fact, by sufficiently increasing the convective velocity $v$, the two regions can be even merged into one large region.

## 5   Discussion and conclusions

A systematic approach combining stability analysis of complex reaction networks and reactor dynamics was applied to a cross-flow catalytic tubular reactor for removal of noxious
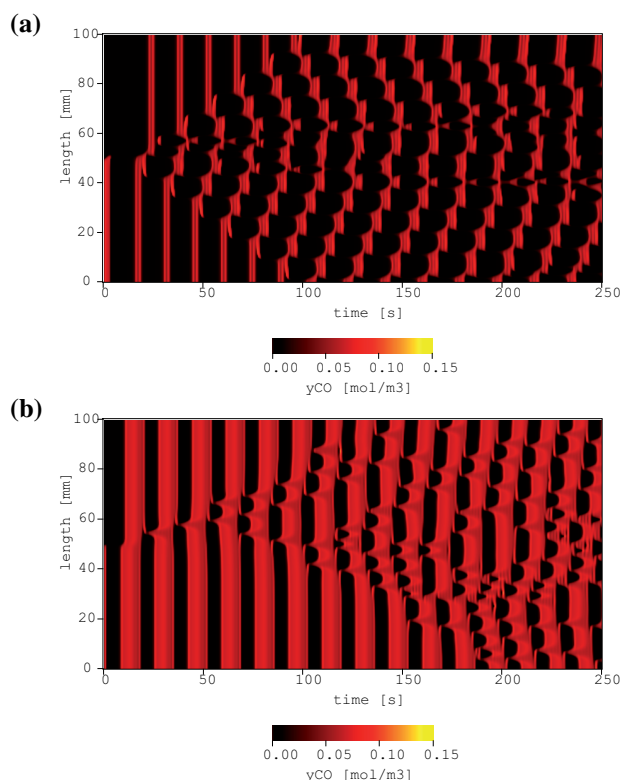
**Fig. 12** The space-time plot of spatiotemporal chaotic pattern; the inlet oxygen concentration (a) – $y_{O_2}^{in}$ = 0.535 mol. % and the temperature $T^{in}$ = 490.0 K, (b) – $y_{O_2}^{in}$ = 0.50 mol. % and $T^{in}$ = 496.0 K, $v = 0$.

components from exhaust gases with the use of a detailed kinetic scheme of simultaneous oxidations of carbon monoxide and acetylene (a representative hydrocarbon) and reduction of nitrogen oxides. To demonstrate various possibilities for oscillatory instabilities and patterns, the system was split into CO & $C_2H_2$ and CO & $NO_x$ subsystems. The stoichiometric network analysis was used to identify positive and negative feedbacks that cause oscillations of reaction components in the lumped model of the reactor. These results were used to explain the structure of the bifurcation diagrams obtained by numerical continuation. In particular, regions of oscillatory dynamics are understood in terms of specific subnetworks involving certain species that play crucial role in the alternating dominance of positive and negative feedback during oscillations. The occurrence of bistability/excitability of steady states is also readily explained by permanent/transient dominance of the corresponding positive or negative feedback loops. We identified these feedback loops for the two examined subsystems.

Our analysis predicts that hydrocarbon involving oscilla-

tions tend to occur at temperatures much higher than oscillations involving nitrogen oxide. The network analysis predicts that the necessary condition for the oscillations in the CO & $C_2H_2$ subsystem is the presence of both Pt and Ce catalytic sites. This is reflected by Fig. 2 shown for the ratio $L_{NM}/L_{OSC}$ = 40/20; any higher value of $L_{OSC}$ yields a similar diagram. On the other hand, the CO & $NO_x$ oscillatory subnetwork (Fig. 9) does not depend on the presence of Ce sites as demonstrated in the bifurcation diagrams (Fig. 8). Moreover, our additional calculations show that oscillations are not suppressed even at much higher values of $L_{OSC}$. Since the same holds also for the sole CO oxidation subsystem[30] we conclude that in all cases the oscillatory dynamics is predicted to persist even for high loadings of Ce oxides as typical of industrial TWC catalysts.

Under the CFR conditions the ranges of oscillatory/bistable/excitable dynamics are quite large and there is a distinct difference in the oscillatory characteristics when the reactor is operating below or above the stoichiometric amount of oxygen. Based on the lumped model analysis, we can make an educated guess of conditions for the CFR to display travelling concentration pulses, fronts and wave trains, and interpret the chemical processes involved in these patterns in terms of the role of specific species found by the reaction network analysis. More subtle features giving rise to complex spatiotemporal patterns result from interplay of reaction and transport under specific constraints. In particular, alternating downstream and upstream wave trains occur near the boundary between excitability and superstoichiometric oscillations but they do not occur at the boundary between excitability and substoichiometric oscillations. This feature is present in both the CO & $C_2H_2$ and CO & $NO_x$ subsystems, but it is much more pronounced in the latter. The alternating waves have been found in other chemical systems under similar constraints[38] and thus the phenomenon seems to be independent of a particular chemistry involved, yet the extent and richness of such dynamics does seem to depend on the topological details of the reaction network. In contrast, spatiotemporal dynamics associated with the substoichiometric oscillatory region display complex, apparently chaotic, patterns which are absent in the superstoichiometric domain. Likewise, this dynamical mode occurs in both subsystems but the complexity in the CO & $NO_x$ subsystem is more varied.

When examining differences in the topological arrangement of the unstable subnetworks that may underlie the subtle differences in spatiotemporal patterns, we find two distinct features: i) NO is the oxidizing agent in the CO & $NO_x$ subsystem ($O_2$ is not involved in the dominant unstable network) which is weaker oxidant than oxygen in the CO & $C_2H_2$ subnetwork and that makes the autocatalysis in the CO & $NO_x$ oscillator weaker and more prone to transport-induced perturbations; ii) there are two autocatalytic loops in the CO & $NO_x$

subsystem, one involving CO oxidation and the other NO reduction, which operate in synergy in the lumped system but may become desynchronised when transport is involved. We conclude that even though the complex spatiotemporal patterns are to a significant degree independent of the chemistry (provided that it is autocatalytic and displays bistability/excitability/oscillations), the robustness of the underlying dominant oscillatory subnetwork does affect the complexity of patterns.

# References

1 M. Sheintuch and N. I. Jaeger (Eds), *Catalysis Today*, 2001, **70**, 285–426.

2 H. H. Rotermund, W. Engel, M. Kordesch and G. Ertl, *Nature*, 1990, **343**, 355–357.

3 R. Imbihl and G. Ertl, *Chemical Reviews*, 1995, **95**, 697–733.

4 M. M. Slinko, *Catalysis Today*, 2010, **154**, 38–45.

5 H. Beusch, P. Fieguth and E.Wicke, *Chemie Ingenieur Technik*, 1972, **44**, 445–451.

6 E. Eckert, V. Hlaváček and M. Marek, *Chemical Engineering Communications*, 1973, **1**, 95–102.

7 J. Kapička and M. Marek, *Surface Science*, 1989, **222**, L885–L889.

8 J. Kapička and M. Marek, *Journal of Catalysis*, 1989, **119**, 508–511.

9 M. Sheintuch and O. Nekhamkina, *Catalysis Today*, 2001, **70**, 369–382.

10 O. Nekhamkina and M. Sheintuch, *Chemical Engineering Science*, 2007, **62**, 4948–4953.

11 M. Sheintuch and O. Nekhamkina, *AIChE Journal*, 2003, **49**, 1241–1249.

12 R. M. Heck, J. Wei and J. R. Katzer, *AIChE Journal*, 1976, **22**, 477–484.

13 S. H. Oh and J. C. Cavendish, *Industrial & Engineering Chemistry Product Research and Development*, 1982, **21**, 29–37.

14 K. Zygourakis and R. Aris, *Chemical Engineering Sciences*, 1983, **38**, 733–744.

15 E. Tronconi and P. Forzatti, *AICHE Journal*, 1992, **38**, 201–210.

16 A. B. K. Lie, J. H. B. J. Hoebink and G. B. Marin, *Chemical Engineering Journal and the Biochemical Engineering Journal*, 1993, **53**, 47–54.

17 P. Pinkas, D. Šnita, M. Kubíček and M. Marek, *Chemical Engineering Sciences*, 1995, **49**, 5347–5358.

18 T. Kirchner and G. Eigenberger, *Chemical Engineering Sciences*, 1996, **51**, 2409–2418.

19 V. Balakotaiah, N. Gupta and D. H. West, *Chemical Engineering Science*, 2000, **55**, 5367–5383.

20 D. Chatterjee, O. Deutschmann and J. Warnatz, *Faraday Discussions*, 2002, **119**, 371–384.

21 L. S. Mukadi and R. E. Hayes, *Computers & Chemical Engineering*, 2002, **26**, 439–455.

22 P. Kočí, M. Kubíček and M. Marek, *Industrial & Engineering Chemistry Research*, 2004, **43**, 4503–4510.

23 A. Güthenke, D. Chatterjee, M. Weibel, B. Krutzsch, P. Kočí, M. Marek, I. Nova and E. Tronconi, *Advances in Chemical Engineering*, 2007, **33**, 103–211.

24 O. Hadač and I. Schreiber, *Phys. Chem. Chem. Phys.*, 2011, **13**, 1314–1322.

25 B. L. Clarke, *Advances in Chemical Physics*, 1980, **43**, 1–278.

26 J. Ross, I. Schreiber and M. O. Vlad, *Determination of Complex Reaction Mechanisms*, Oxford University Press, Inc., New York, 2006.

27 R. H. Nibbelke, A. J. Nievergeld, J. H. Hoebink and G. B. Marin, *Applied Catalysis B: Environmental*, 1998, **19**, 245–259.

28 J. M. Harmsen, J. H. Hoebink and J. C. Schouten, *Chemical Engineering Science*, 2001, **56**, 2019–2035.

29 J. M. Harmsen, J. H. Hoebink and J. C. Schouten, *Catalysis Letters*, 2001, **71**, 81–90.

30 M. Marek, M. Schejbal, P. Kočí, V. Nevoral, M. Kubíček, O. Hadač and I. Schreiber, *Chaos*, 2006, **16**, 1–13.

31 O. Hadač and I. Schreiber, *to be submitted to Journal of Physical Chemistry*, 2015.

32 P. Kočí, V. Nevoral, M. Záhrubský, M. Kubíček and M. Marek, *Chemical Engineering Sciences*, 2004, **59**, 5597–5605.

33 M. Kubíček and M. Marek, *Computational methods in bifurcation theory and dissipative structures*, Springer Verlag, New York, 1983.

34 M. Kohout, I. Schreiber and M. Kubíček, *Computers & Chemical Engineering*, 2002, **26**, 517–527.

35 M. Marek and I. Schreiber, *Chaotic Behaviour of Deterministic Dissipative Systems*, Cambridge Univ. Press, Cambridge, 1991 and 1995.

36 M. Eiswirth, A. Freund and J. Ross, *Advances in Chemical Physics*, 1991, **80**, 127–199.

37 M. Eiswirth, A. Freund and J. Ross, *Journal of Physical Chemistry*, 1991, **95**, 1294–1299.

38 T. Trávníčková, *Ph.D. thesis*, Institute of Chemical Technology, Prague, 2009.